Journal of Manufacturing Processes
Vol. 6/No.2
2004

Modeling Schemes, Transiency, and Strain Measurement for Microscale Laser Shock Processing

Hongqiang Chen and **Y. Lawrence Yao,** Dept. of Mechanical Engineering, Columbia University, New York, New York, USA

Abstract

In this paper, a coupled modeling scheme, which considered the dynamic evolution of laser-induced plasma and the complete physical interaction between the plasma, confined medium, coating layer, and processed metal, is compared with two decoupled modeling schemes in which shock pressure was first determined and used as loading in subsequent FEM-based stress/strain analysis. The relative merits and limitations of these schemes are evaluated in terms of their ability to describe process transiency such as shock pressure, shock velocity, and dynamic deformation history and to predict the stress/strain to be imparted into a target material. Both bulk and thin-film samples of copper were studied. Model predictions were investigated together with strain measurements based on an X-ray microdiffraction technique.

Keywords*: Laser-Induced Plasma, Shock Wave Evolution, FEM Simulation, X-Ray Microdiffraction*

1. Introduction

Laser shock processing (LSP) has been studied since the 1960s (White 1963; Clauer and Holbrook 1981; Peyre et al. 1998). Laser-generated shock waves in a confining medium have been used to improve the mechanical properties of various metals such as aluminum, steel, and copper. In particular, LSP can induce compressive residual stresses in the target and improve its fatigue life, which is important in applications such as turbo blades of an aircraft engine. Earlier modeling work on LSP was carried out by Clauer and Holbrook (1981). Fabbro et al. (1990) developed a model assuming that a certain amount of plasma exists instantaneously once the laser is on and that the process is time dependent only and not spatially dependent. The dynamic deformation process of the target material under the action of shock load had been simulated using the finite element method (FEM) (Peyre et al. 1995; Berthe et al. 1998).

The expanding applications of microdevices make the mechanical properties of such devices an increasing concern. Failure and reliability problems in MEMS have attracted increasing attention recently (Miller et al. 1998; Tanner et al. 2000; Que et al. 2000). In metal structures experiencing rubbing or cyclic loading (mechanical or thermal), such as microelectromechanical actuators, micro-gears, micro-switches, and microchannels, wearing and fatigue performance of the metal structure should be improved to increase the reliability of the system.

More recently, laser shock processing of aluminum and copper using a micron-sized beam has been studied (Zhang and Yao 2000a, b; Zhang and Yao 2001a, b). It has been shown that microscale laser shock processing can efficiently induce favorable residual stress distributions in bulk metal targets with micron-level spatial resolution. Modifications in the modeling of LSP were made from Fabbro's model to account for the microscale involved (Zhang and Yao 2000a, b). A further improvement of the pressure model, taking into account mass, energy, and momentum conservation, was carried out with the plasma modeled as a laser-supported combustion wave and its spatial expansion effects accounted for (Zhang and Yao 2001b). A dynamic deformation process of the target material under the action of shock load had been simulated using the finite element method (FEM) for the axisymmetric case (Zhang and Yao 2000a, b) where semi-infinity boundary conditions were implicitly assumed. The stress and strain analysis was extended to 3-D, and finite geometry was considered, which again is important for microscale LSP (Zhang and Yao 2001b). The micro scale poses challenges in the characterization of the stress/strain fields. Conventional X-ray diffraction does not provide the spatial resolution necessary to characterize the residual stress distribution. High-spatial resolution characterization of the stress/strain fields in thin films was presented in Zhang and Yao (2002).

However, there exist limitations in the work on microscale LSP. It was assumed that the plasma generated in laser shock processing obeys ideal gas laws and that the laser irradiation absorption is a constant. It was also assumed that density, internal energy, and pressure of the plasma are uniform within the plasma volume and vary with time only. To simplify the calculation, the coating layer was considered to be thin and well coupled with the metal target; thus, the shock pressure and the particle velocities of the coating layer and the metal target are identical. The modeling is decoupled in which the shock pressure was computed first from the pressure model and then used as loading for the strain/stress analysis via the FEM code, assuming that the mechanical deformation will not affect the pressure evolution. In fact, the process is coupled. The objective of this paper is to investigate ways to overcome these limitations.

2. Coupled Modeling of Laser Shock Processing

To overcome the limitations of the previous modeling work, a coupled model with a hydrodynamic approach is presented here. The dynamic evolution of plasma and the complete physical interaction between plasma, confined medium, coating layer (ablator), and processed metal (target) are considered as a whole. The shock pressure can be considered very high and much larger than the yield stress of the material. So the strength effects may be neglected and the target material can be treated as an inviscid compressible fluid, which is known as the "hydrodynamic" approach. The dynamic material deformation history, shock wave evolution, and shock pressure can be obtained simultaneously compared to the decoupled model, which uses shock pressure as loading in FEM analysis and assuming that the mechanical deformation will not affect the pressure evolution.

2.1 Physical Phenomena in LSP

The mechanism of forming a high-temperature, high-pressure plasma is as follows. Laser absorption in the ablator occurs within a skin depth that has a thickness measured in tens of angstroms (Guy 1989). Therefore, only a very thin surface layer of the ablator material is heated by the laser light. Because of the rapid energy deposition time, thermal diffusion of energy away from the interaction zone is limited to, at most, a few micrometers. The heated material vaporizes and the vapor rapidly achieves temperatures greater than several tens of thousands of degrees; the generation of a large concentration of electrons above the surface due to thermion emission has often been considered as the cause of plasma ignition (Guy 1989). At first, electron-neutral inverse Bremsstrahlung or multi-photon ionization (for short wavelengths such as UV laser) contributes to the creation of initial electrons. When sufficient electrons are generated, the dominant laser absorption mechanism makes a transition from electron-neutral inverse Bremsstrahlung to electron-ion inverse Bremsstrahlung. So the laser absorption of the vapor becomes much stronger and the vapor is rapidly transformed into the plasma. This plasma induces shock waves during expansion from the irradiated surface, and mechanical impulses are transferred to the target. The plasma-target interaction can be modeled as a hydrodynamic motion under very high pressure and temperature. If the plasma is not confined, that is, it is in open air, the pressure can only reach several tenths of one GPa when the surface is irradiated by a laser pulse of, say, 1 GW/cm^2. If the plasma is confined by water or other media, the shock pressure can be magnified by a factor of five or more compared with the open-air condition (Fox 1974). At the same time, the shock pressure lasts two to three times longer than the laser pulse duration.

2.2 Governing Relations in LSP

Laser absorption in LSP: As for the plasma absorption, the so-called inverse Bremsstrahlung mechanism of the ionization is dominant, and one part of the laser energy is used to increase the thermal internal energy of the plasma (increase the plasma pressure). The other part of the laser energy is used for plasma ionization. The absorption coefficient, α_p, changes with the temperature, and a different equation, (1) or (2), should be used according to different temperature.

At temperatures less than 10,000 K, only a few electrons are present and electron-neutral inverse Bremsstrahlung dominates. The effective absorption coefficient is given by (Robert 1989):

$$\alpha_p = \left[1 - \exp(-\frac{hc}{\lambda kT})\right] \sum_j Q_j n_e n_j \qquad (1)$$

where n_e and n_j are the number density of the electron and the *j*th neutral atomic species, respectively, Q_j is the average cross section for absorption of a photo of wavelength λ by an electron during a collision with species *j*, *k* is Boltzmann's constant, *h* is Planck's constant, *c* is velocity of light, and *T* is temperature. When temperature gets higher and the more electrons are generated, electron-ion inverse Bresstrahlung dominates. The effective absorption coefficient is:

$$\alpha_p = \left[1-\exp(-\frac{hc}{\lambda cT})\right]\frac{4e^6\lambda^3}{3hc^4m_e}(\frac{2\pi}{3m_ekT})^{\frac{1}{2}}n_e\sum_j z_i^2 n_i g_i \quad (2)$$

where z_i and n_i are the charge and number density of the *i*th ionic species, respectively, g_i is the appropriate Gaunt factor that corrects the semi-classical expression for quantum effects, and m_e is the mass of the electron.

Ionization model: Because the laser pulse width in LSP is 50 ns in this study, which is much larger than the electron-ion collision time, τ_{ei}, the ion formation can be treated within the framework of the local thermal equilibrium theory (LTE) and it is possible to employ the Saha relations (Mitchner and Kruger 1973).

$$\frac{n_e n_1^+}{n_k} = 2\frac{g_l^+}{g_k}(\frac{2\pi m_e kT}{h^2})^{3/2}e^{-\varepsilon_{k\lambda}/kT} \quad (3)$$

where n_e is the free electron number density, n_1^+ is the number density of single ionized positive ions in the ground level, and n_k is the number density of neutral particles in the *k*th level. Here is assumed an equilibrium between electrons, ions, and neutrals, and the electron and ion density are always equal. The Saha-Eggert equation was used and the degree of ionization was given by:

$$\frac{\eta^2}{1-\eta^2} = \frac{m}{\rho}(\frac{2\pi kTm_e}{h^2})^{3/2}\exp(-\frac{U}{kT}) \quad (4)$$

where m_e is the mass of the electron, *m* denotes the mass of the particles, *k* is the Boltzmann constant, and *U* is the ionization potential of the target material (*U* = 5.989 eV for the Al coating layer). The degree of ionization, $\eta = \frac{n_i}{n_{total}}$, is expressed by the number density ratio of ions and all particles. Some other ion models, such as the Thomas-Fermi model, which is based on Fermi-Dirac statistics and is particularly good for metals, or the average-atom model, which is relevant to dense plasmas, have also been used in LSP modeling depending on the materials involved and process conditions used.

Hydrodynamics: After the creation of the plasma, the expansion of the high-pressure plasma drives a shock wave into the target and the confining medium in two opposite directions. The interface movement between plasma and the target and confining medium can be treated as the hydrodynamic motion behind the two shock waves that are propagating inside the target and confining medium. For the plasma itself, it is also possible and advantageous to view the plasma as a continuum, or fluid. A sufficient condition for the applicability of such a description is that the plasma be collision dominated (Mitchner and Kruger 1973). By this it is meant that the mean free paths for particle collisions for all species be much smaller than the characteristic length scale for macroscopic change, and that the particle collision intervals be much smaller than the characteristic time scale for macroscopic change. So, one can adopt a primarily macroscopic approach here and the hydrodynamic motions are redescribed by the conservation of mass, momentum, and energy. For simplification, only the one-dimensional hydrodynamic governing equation is shown (Vertes et al. 1989):

$$\frac{\partial\rho}{\partial t} = -\frac{\partial(\rho v)}{\partial x} \quad (5)$$

$$\frac{\partial(\rho v)}{\partial t} = -\frac{\partial(p+\rho v^2)}{\partial x} \quad (6)$$

$$\frac{\partial[\rho(e+v^2/2)]}{\partial t} = -\frac{\partial[\rho v(e+p/\rho+v^2/2)]}{\partial x} + \alpha\Phi \quad (7)$$

where ρ is density, *v* is velocity, *e* is internal energy, *p* is pressure, and Φ is input laser intensity. From the ideal gas law, there is the well-known form:

$$p = (1+\eta)\frac{pkT}{m} \quad (8)$$

where η is the degree of ionization.

The conservation equations of mass, momentum, and energy can be closed by a constitute equation, which relates the physical parameters of the mate-

rial. The simplest equation of state is governed by the ideal gas law (Vertes et al. 1989):

$$\rho e = \frac{\rho}{m}[\frac{3}{2}(1+\eta)kT + \eta U] \quad (9)$$

where e is the internal energy and m is the mass of the particles. More reliable equations of state for different materials can be based on the tabulated form such as the Los Alamos Sesame Library. In such a table, plasma pressure p and internal energy e can be obtained as the dependent of temperature T and plasma density ρ. Because an equilibrium is assumed between electrons, ions, and neutrals and only one type of neutral atomic species is considered, in Eq. (1), $j = 1$, the electron number density $n_e = n_{total}\ \eta$, and the number density of neutral is $n_n = n_{total}\ (1 - \eta)$. Similarly, in Eq. (2), $i = 1$ and the charge density $z_i = n_e = n_i = n_{total}\ \eta = \rho\eta/m$. Thus, there are seven unknowns, ρ, v, p, e, T, η, and α_p in seven equations, (1) or (2) and (4)–(9). The finite-difference method is used to solve those unknowns through those equations. Numerical values for all parameters used in equations have been given in a table in the Appendix.

3. Simulation and Experiment Condition

The coupled analysis of shock pressure generation and dynamic deformation process of the target material subjected to LSP was carried out. The simulation results were compared with that from two decoupled analysis schemes, in which shock pressure generated either based on the above model or the model (Zhang and Yao 2001b) is used as loading in a subsequent FEM deformation analysis. The coupled analysis was implemented using a commercial radiation hydrodynamics simulation code, HYADES (Hyades 2001). HYADES is a one-dimensional, Lagrangian hydrodynamics and energy transport code, designed for high temperature applications such as that in the laser-material interaction, where materials are significantly ionized. The temporal and spatial change of pressure, density of different mesh zones in the depth direction can be tracked. Different materials in different regions can be defined and so it is convenient to solve multiplayer LSP problems such as thin-film/substrate targets. Moreover, the hydrodynamic code incorporates deformation analysis so the dynamic deformation result can be obtained together with other physical parameters such as pressure, temperature and density. Thomas-Fermi model was used for ionization in copper and aluminum regions because it is more appropriate for metals. As for the confinement medium, water, Saha model was used. Models for equation of state of Cu, Al and water are selected from material tables from the Los Alamos Sesame Library. Room temperature is selected for the floor temperature of electron and ion in sample material.

For the decoupled analysis, the model (Zhang and Yao 2001b) assumed that density, internal energy and pressure of the plasma are uniform within the plasma volume and the plasma's absorption of laser energy is a constant. The time history of the shock pressure was then used as loading in a subsequent stress/strain analysis. The deformation analysis was carried out using ABAQUS. Axisymmetric models with semi-infinite geometry were created for bulk targets (Zhang and Yao 2001a), and 3-D models with finite geometry were created for targets made of copper thin films on silicon substrate (Zhang and Yao 2002). A second type of comparison was also carried out, in which HYADES generated shock pressure was used as loading in a subsequent FEM stress/strain analysis. In the FEM simulation, nonlinear constitutive equations including work hardening, strain rate and pressure effects on yield strength of copper target are considered (Zhang and Yao 2000a) assuming room temperature because most heat generated by coating layer ablation is shielded from the target by the layer.

Both bulk and thin-film samples of copper were studied. Copper foils of 90 micron thickness were used as bulk samples. Thin-film samples are prepared by physical vapor deposition (PVD) for 1 μm thick copper film and electrochemical plating (ECP) for 3 μm thick copper film on 0.5 mm thick single-crystal (004) silicon substrate. A 16 micron thick aluminum foil was used as the ablative coating layer for both bulk and thin-film cases and foil was firmly attached to targets using vacuum grease. As seen in *Figure 1*, a sample was placed in a shallow container filled with distilled water around 3 mm above the sample's top surface. A frequency tripled Q-switched Nd:YAG laser (wavelength 355 nm) in TEM mode was used, the pulse duration was 50 ns, and pulse repetition rate could vary between 1 KHz to 20 KHz. Laser beam diameter is 12 microns and laser intensity was varied from 2 to 6 GW/cm^2.

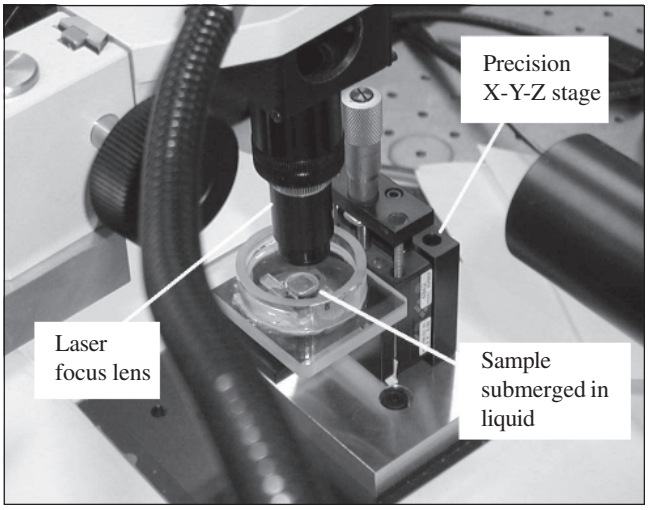

Figure 1
LSP Experiment Setup

As mentioned above, the plasma temperature and pressure in simulation is time and spatially resolved (one dimensional). The plasma temperature can be obtained by spectroscopic measurements but the result is not spatially resolved, especially for the 12 μm laser spot size in microscale laser shock processing. Also the response of spectroscopic measurement may be inadequate for the short laser pulse duration (50 ns). The plasma pressure can be measured with synthetic X-cut quartz crystals and its response is adequate for nanosecond laser pulse. Typically, the quartz crystal is attached firmly to the backside of shocked sample, and the sample should be a foil and can not be too thick (< 10 μm) to affect the response. Thus, we need to use a thin-foil like sample and change the sample thickness that we would like to investigate (90 μm for bulk sample). For the thin-film sample, the thickness of the silicon substrate is 0.5 mm and it cannot be made as a very thin foil. Due to those limitations, we did not choose to measure the plasma temperature and pressure directly and the model can be validated by X-ray diffraction measurement for the LSP-induced strain in the sample predicted by simulation. Traditional X-ray diffraction is limited by its spatial resolution (in the order of millimeters) and cannot be applied to measure the microscale strain distributions generated by microscale LSP. Recent developments in X-ray microdiffraction provide the possibility of measuring the stress/strain fields with micron-level spatial resolution. The X-ray microbeam system in the National Synchrotron Light Source was used in this study and more details will be provided in Section 5.

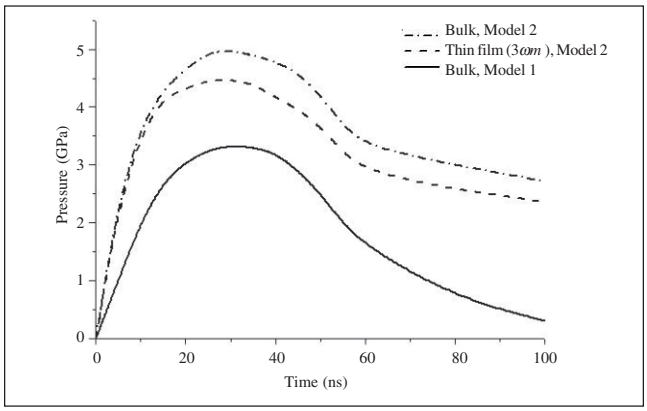

Figure 2
Pressure of Plasma in LSP from Different Models and Samples (Laser intensity I = 4 GW/cm^2)

4. Results and Discussion

4.1 Shock Pressure Comparison from Different Modeling Schemes

To facilitate discussions, the model (Zhang and Yao 2001b) used in the decoupled analysis is denoted as Model 1, while the coupled modeling as Model 2. *Figure 2* compares the shock pressures between these two models under the same laser intensity (I = 4 GW/cm^2). In Model 2, both bulk and thin-film targets were considered and for the thin-film target two different tabular equations of state were used for the film and substrate, respectively. As seen in *Figure 2*, the shock pressure is higher and lasts longer as predicted by Model 2 than that by Model 1. Model 1 assumes that part of the laser energy is used for the breakdown of water and target besides the expansion of plasma. So the more mass flows from water and target into plasma due to breakdown, the less laser energy converts into the internal energy in the plasma. As a result, the pressure of plasma is lower and reduces to the atmosphere value faster. In *Figure 3*, the density of different regions of water and Al coating layer are compared and it shows that the top layer of Al (zone 0) is changed into the plasma as evidenced by the fast density decrease, while the region 1 μm below the top layer (zone –1) can be regarded as the molten layer and the zone –2 (2 μm below the top layer) is still in solid state. For the water, the region near the top Al layer (zone 0 of water, 2 μm thick) can still be regard as liquid that did not change into the plasma. Thus, the plasma generated in Model 2 is mainly from the breakdown of the Al coating layer and not from water. How-

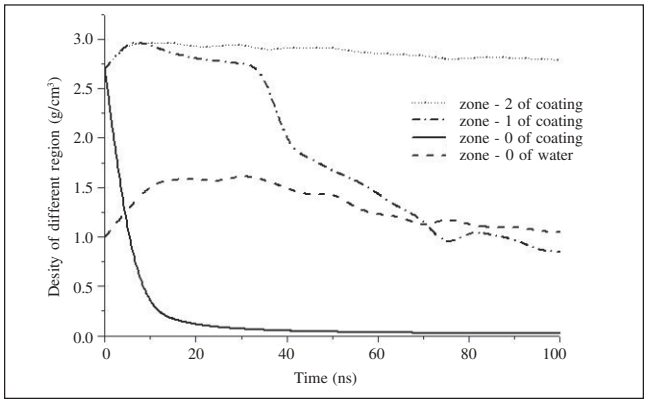

Figure 3
Density at Different Depths of Coating Layer and Confined Medium (zone –2 of coating: 2 μm below the coating surface; zone –1 of coating: 1 μm below the coating surface; zone 0 of coating: coating-water interface, in coating; and zone 0 of water: coating-water interface, in water)

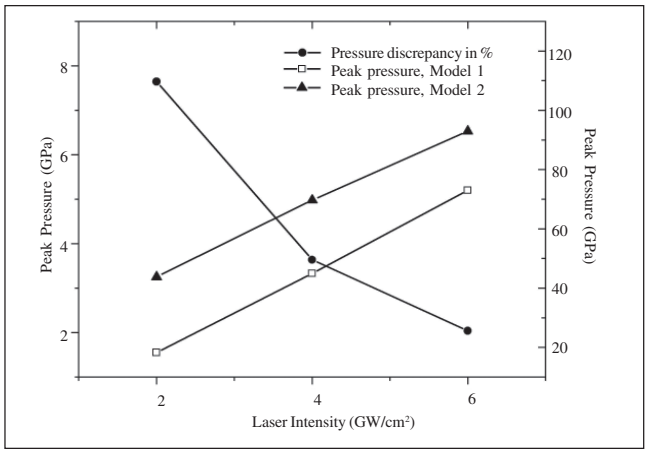

Figure 4
Peak Pressure Comparison of Bulk Material from Model 1 and Model 2

ever, in Model 1, the mass flow from the water is one magnitude higher than from the metal target (Zhang and Yao 2001b) so that much more laser energy was used to breakdown the water to generate the plasma, so the shock pressure is lower than that in Model 2 and it decreases much faster as well.

The pressure difference between these two models can be better explained considering the physical phenomena discussed in Section 2. At short laser wavelengths such as 355 nm used in this study, multiphoton-ionization (MPI) is dominant in the laser water interaction (Berthe et al. 1999). This means the water can be ionized by a sufficient number (m) of photons as

$$M + mhv \rightarrow e^{+} + M^{+} \tag{10}$$

where M is an atom or molecule. At $\lambda = 355$ nm, only four photons are required to ionize single water molecules, which have an ionization energy of 12.6 eV. Thus, the energy needed for directly ionizing the water and converting it into the existing plasma is around 67,500 kJ/kg. However, in Model 1, the energy used to convert water to plasma was simply considered as the liquid to vapor (which is not quite the plasma yet) phase change energy, that is around 2,212 kJ/kg (Zhang and Yao 2001b) and much lower than that in the direct ionization case. For the metal target, Model 1 also considers the mass flow as the phase change energy from the liquid (molten metal) to vapor and its value is around 6,418 kJ/kg, not much lower than the ionization energy of Al (11,872 kJ/kg) used in Model 2. So the water is more likely to convert into the plasma in Model 1 and generates a higher mass flow from water to the "plasma," which is not realistic.

In Model 1, only one type of target material can be considered, and it cannot be used to model the complex multilayer thin-film sample, which is very common in the MEMS field and also important in microscale LSP. However, in Model 2, thin-film samples can be readily modeled by defining different meshes and regions for different material layers. From *Figure 2*, it shows that the peak pressure is slightly lower than that in the bulk sample case, both obtained from Model 2. That is because the single-crystal silicon substrate has lower shock impedance than copper so the plasma and shock wave will expand faster, and there is a material discontinuity between the 3 μm copper thin film and the silicon substrate, which will cost some plasma energy when the shock wave passes through it. Thus, the shock pressure is slightly lower in the thin-film sample than in the bulk sample.

In *Figure 4*, the peak pressure values under different laser intensity obtained using Model 1 are compared with those obtained using Model 2. As discussed earlier, the peak value from Model 2 is higher than that from Model 1. However, such discrepancy decreased from 110% to 25% when laser intensity increased from 2 to 6 GW/cm^2. This is because, when the laser intensity increases, the ionization level of water becomes higher (*Figure 5*) and some water near the plasma can be broken down, thus generating a mass flow into the plasma as assumed in Model 1. So the pressure predicted by the two models gets closer as laser intensity increases.

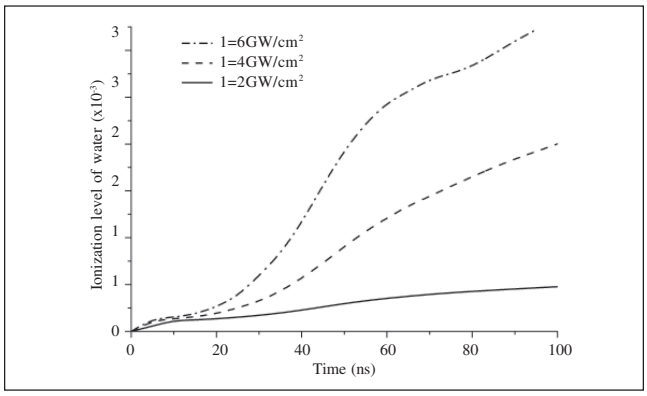

Figure 5
Ionization Level of Water at Coating-Water Interface Under Different Laser Intensity (I = 2, 4, and 6 GW/cm^2)

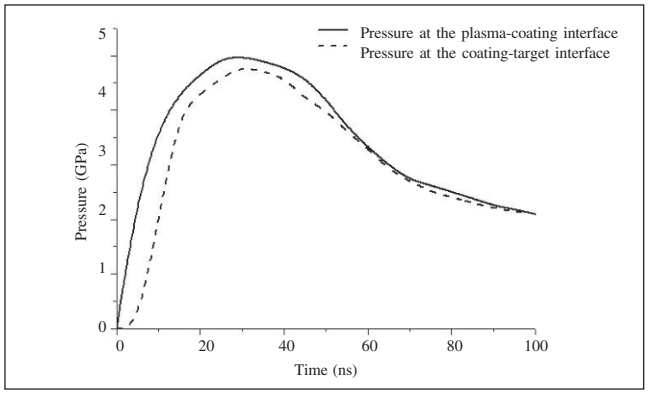

Figure 6
Shock Pressure Attenuation Predicted by Model 2 Across 16 μm Al Coating Layer (bulk copper sample, I = 4 GW/cm^2)

4.2 Transient Processes and Deformation History in Target

The transient processes in laser shock processing are important in order to study the laser-induced shock wave and the dynamic deformation in the target material. From the particle velocity and density change of different zones in the target depth direction, the dynamic evolution of the shock wave can be studied.

Pressure attenuation through the coating layer: In Model 1, the pressure of plasma is considered as the pressure directly applied onto the target. However, when the plasma-induced laser shock wave passes through the Al coating layer, the pressure will be slightly attenuated. In Model 2, the pressure distribution in the depth direction can be obtained directly so that the attenuated shock pressure at the interface of coating layer and the copper target can be determined and continuously used either in the coupled analysis or as loading in a subsequent FEM stress/strain analysis.

Figure 6 shows the pressure attenuation in Model 2 after the plasma-induced shock wave passes through the Al coating layer. The laser intensity is 4 GW/cm^2 and the thickness of the coating layer is 16 μm. The pressure attenuation is about 0.2 GPa for the bulk samples. In *Table 1*, shock pressure attenuation under different laser intensities (I = 2, 4, and 6 GW/cm^2) are compared. As seen, pressure attenuation decreases from 0.25 to 0.1 GPa when the laser intensity increases. According to the analysis of Boslough and Asay (1992), the shock impedance increases with initial shock pressure. Thus, under a high laser intensity, the shock impedance of the coating layer is higher so that the pressure attenuation across it is larger. For thin-film samples, the attenuation values are nearly the same as the bulk samples due to the same coating layer used.

Deformation history analysis: to study the dynamic deformation history in the target material (copper), as mentioned in Section 3, both coupled and decoupled methods are applied here. The coupled method determines the history of deformation, density, and pressure directly from Model 2. In the decoupled method, shock pressure is calculated either from both Model 1 and Model 2 and then used as loading in a subsequent FEM simulation. From Model 1, the pressure is from the plasma and target interface, while in Model 2 the pressure at the coating target is used. *Figures 7* and *8* show typical FEM-predicted deformation results in the depth direction for copper bulk and thin-film samples with pressure loading from Model 1. Axisymmetric modeling is carried out, also assuming semi-infinity in the radial direction. For the thin-film samples, both displacement and normal stress are considered continuous across the copper-silicon interface. As seen from *Figure 7*, the vertical deformation reaches about 30 microns into the bulk sample and the maximum deformation is around 1.8 μm at the top surface. Such deformation also covers a region around 15 μm in radius. For the thin-film sample in *Figure 8*, the ver-

Table 1
Shock Pressure Attenuation Across 16 μm Al Coating Layer Under Different Laser Intensity in Bulk and Thin-Film Sample

Laser Intensity (GW/cm^2)	Bulk		Thin-Film
Samples (GPa)	2	0.12	0.13
	4	0.19	0.2
	6	0.24	0.26

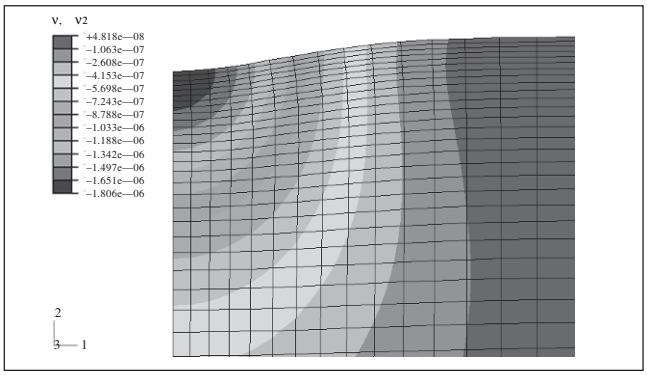

Figure 7
Typical FEM Simulation Result of Vertical Displacement (the 2-direction) in Copper Bulk Sample (Laser intensity I = 4 GW/cm^2, laser beam diameter = 12 μm. Computation domain is 100 μm by 1000 μm assuming axisymmetry. The region shown is 15 μm by 20 μm.)

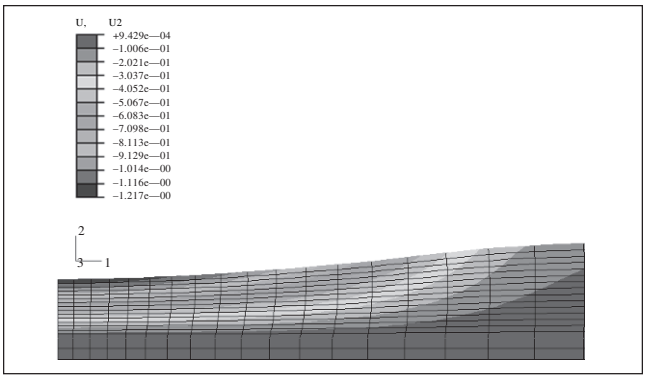

Figure 8
Typical FEM Simulation Result for Vertical (the 2-direction) Deformation in 3 μm Copper Thin-Film Sample (Laser intensity I = 4 GW/cm^2, laser beam diameter = 12 μm. Computation domain is 50 μm by 200 μm assuming axisymmetry. The region shown is 5 μm by 15 μm.)

tical deformation is primarily confined in the 3 μm copper thin film. Very little deformation is seen in the silicon substrate due to its higher Young's modulus than copper. The maximum deformation in copper thin film is around 1.25 μm at the top surface, and the radius of deformation region is also about 15 μm.

Figure 9 shows the transient deformation of the top surface of a copper sample under LSP predicted by different modeling schemes. The results directly from Model 2 is compared with the top surface displacement from the result of FEM simulation with the shock pressure of Models 1 and 2. It shows that the deformation history from FEM simulation using Model 1 and 2 is in the same order and the value of Model 2 is slightly larger due to its higher shock pressure than that of Model 1 (*Figure 2*). When comparing the FEM simulation result with that directly

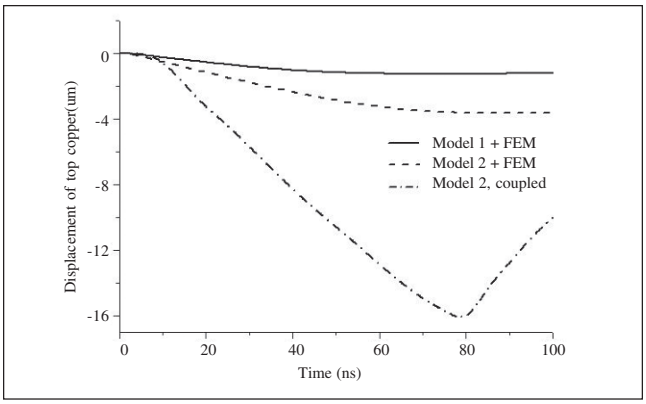

Figure 9
Displacement History of Surface of Copper Target in Bulk Samples (Model 1, decoupled: pressure from Model 1 as loading in FEM; Model 2, decoupled: pressure from Model 2 as loading in FEM; and Model 2, coupled: displacement history directly from Model 2)

from Model 2, a major discrepancy is evident. As seen, during the initial stage of LSP (t < 10 ns, and pressure < 2 GPa), the deformation directly from Model 2 is consistent with the FEM simulation results. However, when time goes on, the deformation determined directly from Model 2 increases much more than FEM simulation results predicted and then rebounds. This can be explained by the different considerations about the material response to shock wave adopted in these two models.

According to Chou (1972), the material response to intensive impulsive loading (such as shock wave induced in LSP) may be described in one of three possibilities, depending on the shock pressure involved: hydrodynamic, finite-plastic, and linear elastic. In Model 2, the shock pressure (2 to 6 GPa) is considered so high that strength effects can be neglected and the target can be treated as a compressible fluid, which is known as the hydrodynamic approach. While in Model 1, shock pressure is used as a loading in FEM simulation, which is based on the finite-plastic approach. Strength effects such as work hardening, strain rate, and pressure effects on yield strength are considered in the FEM simulation (Zhang and Yao 2001b).

In the hydrodynamic approach, the equation of state that relates pressure, density, and energy is used to replace the complicated nonlinear constitutive equations in the FEM simulation. Also, a shock Hugoniot curve can be obtained, in which one property versus others (such as P vs. V) behind the shock is depicted. When the shock pressure is low (i.e., t < 10 ns), the Hugoniot curve is very close to an isotro-

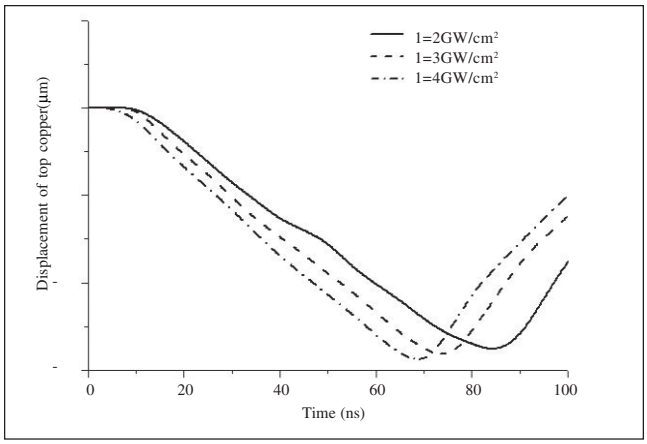

Figure 10
Displacement History of Copper Target Surface of Bulk Sample from Model 2-Based Coupled Analysis Under Different Pressures

pic path, which is usually the case for a solid under impact if the solid is only compressed slightly. Thus, the result from the hydrodynamic approach is consistent with the result from FEM simulation. When time goes on and pressure goes up, the target is compressed more such that both hydrodynamic and strength effect should be considered. The Hugoniot state (P vs. V) will be offset above the hydrostatic Hugoniot (which assumes hydrodynamic approach) due to strength effect (Fowles 1960). Thus, in Model 2, which adopted the hydrodynamic approach, a lower pressure is needed to achieve the same density, so that for the same pressure the material is easier to deform and the top surface displacement will be larger than the FEM simulation result. Moreover, as seen from *Figure 10*, the deformation will become larger when the loading shock pressure goes higher (from 2 to 4 GW/cm^2). This is consistent with the fact that the Hugoniot state will be offset much more under higher pressure loading so that the material is easier to deform (*Figure 11*).

Figure 12 shows the deformation history for the 1 μm and 3 μm copper thin film predicted by the same simulation methods mentioned above. The deformation determined by the Model 2-based coupled method is again much larger than the decoupled results due to the same reason mentioned above. The deformation in the 3 μm sample is slightly larger than in the 1 μm sample from the decoupled simulation results. This is because a thicker film has a longer time to absorb the shock energy than a thinner film. Moreover, the slope of the deformation history, which equals the particle velocity under shock (480 m/s), is about twice as large as that of the bulk samples

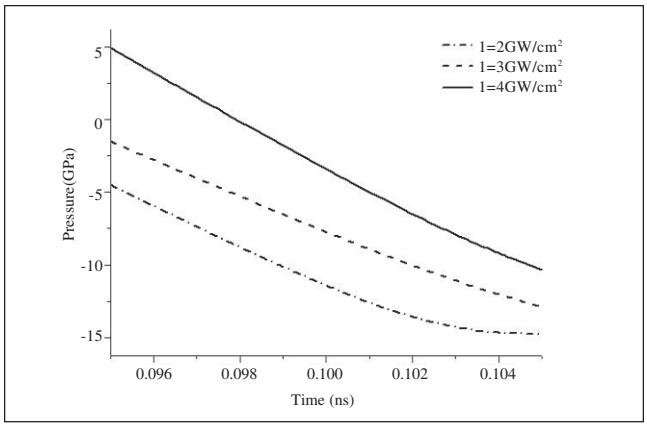

Figure 11
Hugoniot Offset Under Different Pressure: Pressure-Specific Volume Curve

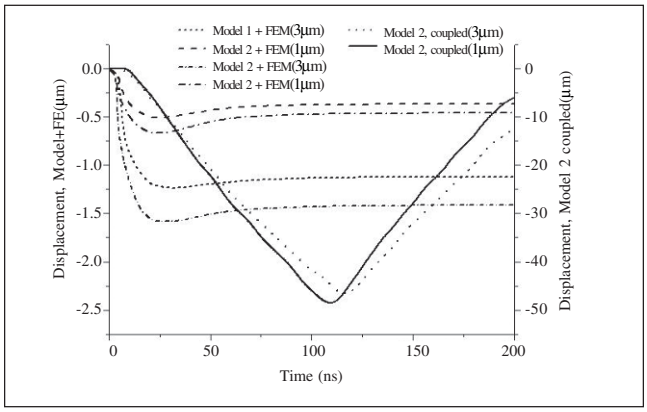

Figure 12
Displacement History at Top Surface of Copper Thin Film for Thin-Film Samples (Laser intensity I = 4 GW/cm^2)

(*Figure 13*). In thin-film samples, the substrate is 200 μm single-crystal silicon as compared to 90 μm copper total thickness in bulk samples. The impedance of single-crystal silicon is about 1.97×10^7 kg/m^{2}s, smaller than that of copper (4.18×10^7 kg/m^{2}s). According to the wave-surface interaction analysis (Boslough and Asay 1992), when shock wave propagates from the high-impedance material (copper thin film here) to the low-impedance material (silicon substrate here), the interaction will result in a reflected release wave back in copper and a transmitted shock in silicon, which has a higher particle velocity due to its lower impedance. Thus, the shock wave can pass through the copper-silicon interface and propagate much easier and the hydrodynamic deformation will be larger than that in the bulk samples.

Laser shock wave propagation: Consider a shock wave passing through the target, the states are undisturbed ahead of the shock front and the target is compressed behind the shock, so shock front posi-

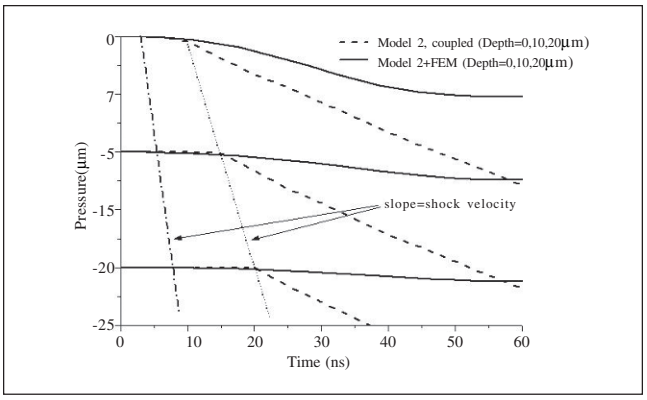

Figure 13
Displacement History in Different Depths of Bulk Copper Target (0, 10, and 20 μm below the top surface, laser intensity I = 4 GW/cm^2)

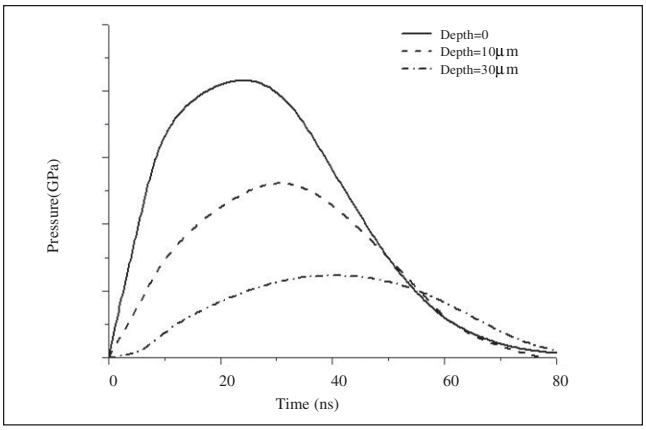

Figure 14
Stress Normal to Top Surface at Different Depths for Bulk Samples Determined by FEM Simulation Using Pressure Loading from Model 2 (laser intensity I = 4 GW/cm^2)

tion and shock velocity can be determined if deformation history in the depth direction is known. In *Figure 13*, the deformation history at different depth levels in the copper target is shown, from which the shock wave velocity can be seen so that the laser shock wave propagation history can be studied. From the Model 2-based coupled analysis, the particle velocity, that is, the slope of the deformation history curve, is about 240 m/s, and the shock velocity, that is, the slope of the straight line that connects the shock front at different times, is about 2 km/s. From the decoupled results, the particle velocity is 120–160 m/s, while the shock velocity is about 4.14 km/s. The discrepancy is explained as follows.

Examining the material response parameters under shock impact, the shock velocity of copper is $U = C_0 + Su$, where C_0 (3.94 km/s) is the sound velocity in copper, $S = 1.489$ (Asay and Shahinpoor 1992), and particle velocity u = 135 m/s under 5 GPa shock pressure as determined above. This gives U = 4.17 km/s, which is very close to that determined by the decoupled analysis shown in *Figure 13*. This is because in the FEM portion of the decoupled analysis, nonlinear constitutive equations including work hardening, strain rate, and pressure effects on yield strength of the copper target are considered and they are comparable with the Hugoniot data obtained from material experiments. In the Model 2-based coupled analysis, the shock velocity (2 km/s) is close to that of water, which is around 2.1 km/s for the same particle velocity. This is because, under the hydrodynamic approach employed by the coupled analysis, the target material is considered as a compressible fluid.

As seen from *Figures 9* and *12*, the deformation curves determined by the Model 2-based coupled analysis reverse their direction at a certain time. This can be explained by the shock velocity analysis above. When a shock front propagates to reach the bottom surface of the target, the rarefaction wave (release wave) is reflected back and this reflected wave generally cancels part of the original incoming shock wave so that the total pressure decreases. In the hydrodynamic approach employed by the Model 2-based coupled analysis, the target material will expand when the pressure decreases by behaving like a compressible fluid or gas. Thus, the deformation reverses its direction at that time. The shock velocity here is about 2 km/s (see analysis above). It takes about 80 ns for the shock wave to propagate to the bottom surface and then reflect back to the top surface of the 90 μm thick bulk copper target. That corresponds to the time when deformation reverses its direction (*Figure 9*). For the thin-film sample shown in *Figure 12*, the direction of deformation reverses at about 115 ns due to the thicker silicon substrate (200 μm) than the bulk sample (90 μm) and larger shock velocity in the silicon substrate (around 3 km/s).

Pressure/stress analysis in the depth direction: Figure 14 shows the history of the stress normal to the sample top surface at different depths of a bulk copper sample obtained from the decoupled analysis with Model 2-determined pressure as loading in a subsequent FEM analysis. *Figure 15* shows the same result determined using the Model 2-based coupled analysis. As seen, stress peak value decays much faster in *Figure 14* than in *Figure 15*. This is because, in the FEM simulation of the decoupled

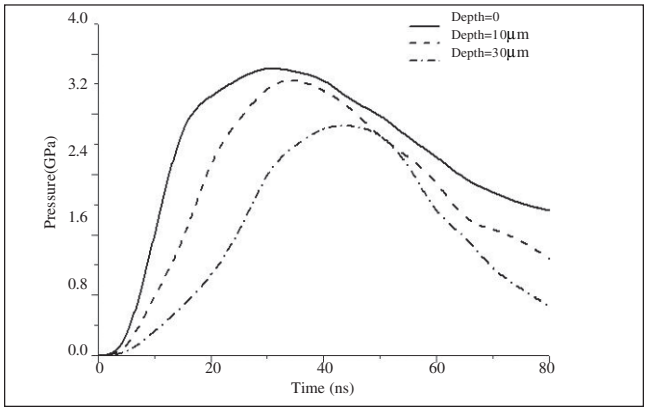

Figure 15
Shock Pressure History at Different Depths of Bulk Samples from Model 2 (laser intensity I = 4 GW/cm^2)

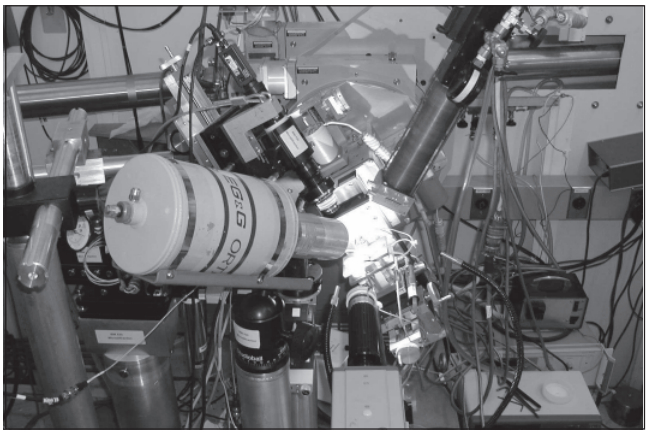

Figure 16
X-Ray Microdiffraction Experiment Setup

analysis, plastic deformation and strength effect are considered so that more work is dissipated on the deformation of the target when the shock wave propagates into the target. While under the hydrodynamic approach employed in the coupled analysis, pressure is determined by the equation of state of the target and the target is considered as an elastically compressible fluid. So no extra work is dissipated on the irreversible plastic deformation and the pressure decay is slower.

Another phenomenon observed in *Figure 14* is the asymmetrical profile of pressure at different depths. When the depth changes from 0 to 30 μm, the steep rising edge, which corresponds to the shock front in the target, shifts from left to right, makes the pressure profile nearly symmetric, and thus no significant shock front can be observed any more. That is because, in the FEM simulation, dissipative mechanisms such as plastic deformation and dynamic yield strength increase prevent the shock from becoming a true, infinitesimally thin discontinuity. So the shock front is hard to observe here. In comparison, the pressure profiles' becoming symmetric is less pronounced in *Figure 15*, where the Model 2-based coupled analysis assumed no such dissipative mechanisms.

5. Strain Measurement via X-Ray Microdiffraction

5.1 Measurement Setup and Principle

LSP-induced strains were measured to compare with that predicted by simulation. Recent developments in X-ray microdiffraction provide the possibility of measuring the stress/strain fields with micron-level spatial resolution. *Figure 16* shows the setup of the X-ray microdiffraction experiment. Experiments were conducted at the X20A beamline of the National Synchrotron Light Source at Brookhaven National Laboratory. The incident X-ray was focused using a tapered glass capillary to form a 10 × 10 μm spot on the sample surface. Thin-film samples after LSP were measured using the diffraction intensity contrast method (Noyan et al. 1998). The samples are either 1 or 3 μm thick polycrystalline copper thin films on single-crystal silicon substrate with (004) orientation. Samples were vacuum-held onto a motorized, high-precision XYZ stage. By scanning the sample relative to the beam in 2-micron step size across the shocked region, Si (004) diffraction from the silicon substrate was collected using a scintillation detector and the distribution of the Si (004) intensity across the shocked region was recorded.

In the diffraction intensity contrast method (Noyan 1998), the X-ray microbeam is so chosen that it penetrates the thin-film polycrystalline copper to reach the silicon substrate and the diffraction intensity of the single-crystal substrate is recorded. The stress/strain in the substrate was coupled to by [delete by?] the LSP-deformed thin film. The increase of diffraction intensity comes from the increased mosaic structure in the substrate under the influence by the stress/strain field in the thin film at the interface (Cullity 1978). An index to evaluate this combined effect is strain energy density D, defined as follows (Ventsel and Krauthammer 2001):

$$D = \frac{1}{2}\varepsilon_{ij}\sigma_{ij} = \frac{1}{2}(\varepsilon_{11}\sigma_{11} + \varepsilon_{22}\sigma_{22} + \varepsilon_{33}\sigma_{33} + \varepsilon_{12}\sigma_{12} + \varepsilon_{13}\sigma_{13} + \varepsilon_{23}\sigma_{23}) \quad (11)$$

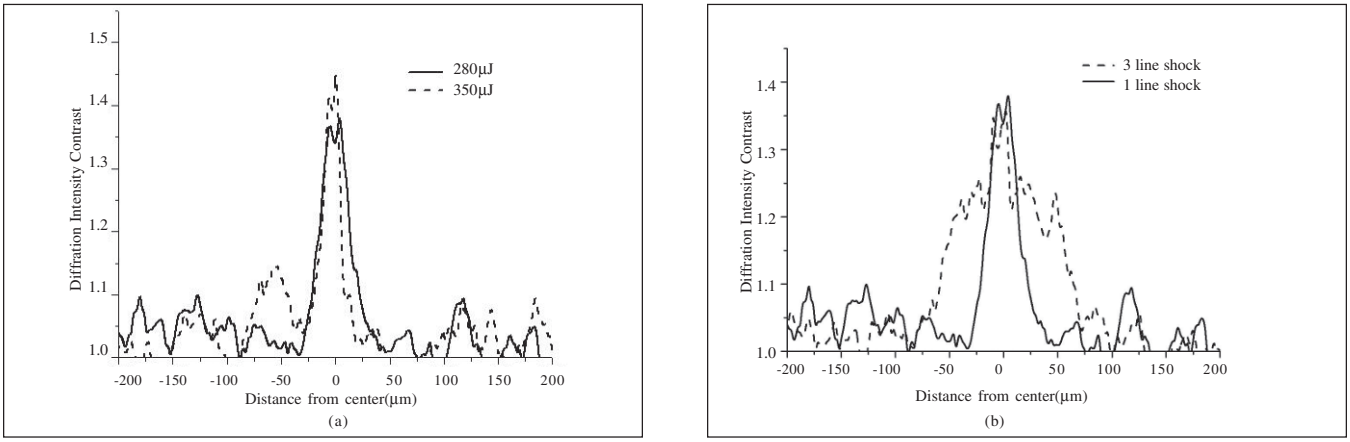

Figure 17
Diffraction Intensity Contrast Across Shocked Region on 1 μm Thick Thin-Film Sample Measured in 2 μm Step Size. (a) 280 and 350 μJ, single-line LSP and (b) comparison of single line and three-line results, 280 μJ. Diffraction intensity is normalized to average background intensity (18,000 counts).

where ε_{ij} is the total strain tensor and s_{ij} is the residual stress tensor at the thin-film/substrate interface. The unit of D is J/m^3. Strain energy density is difficult to measure experimentally, but its value can be extracted from simulation.

5.2 Measurement Results and Comparison with FEM Simulation

The measured diffraction intensity contrast curves are compared with the FEM-determined strain energy density. The plasma pressure determined from the simulation result is used as the loading in the FEM simulation. So the X-ray measurements provide comparisons between simulation and experiment results.

Figure 17 shows the profiles of diffraction intensity contrast measured across the shocked region of the samples. Each sample was shocked along its centerline by a series of laser pulses, with spacing between consecutive pulses being 25 μm. As noted earlier, the laser beam diameter is about 12 microns. The diffraction intensity is normalized to the background diffraction intensity. All the measurements were taken at 2-micron spacing. As seen from *Figure 17a*, a contrast peak stands out at the centerline under both laser energy levels, 280 and 350 μJ, which correspond to 3.89 and 4.86 GW/cm^2, respectively. The contract peak for 350 μJ is higher than that of 280 μJ due to the stronger shock effect. The width of the peaks is around 75 μm. This clearly shows that LSP has imparted significant strain in the samples. *Figure 17b* superimposes the diffraction intensity contrast curve measured from a sample, which was shocked along three parallel lines, onto the curve from a sample that was shocked along only one line. The three parallel shock lines have 50-μm spacing between them with the midline right on the sample centerline. As seen, the peak at the center remains, while two secondary peaks appear in both sides of the main peak at about ±50 μm from the center. This is consistent with the line spacing used in the shocking experiments. The center peak is higher than the secondary peaks due to a level of superposition.

Figure 18 correlates the diffraction intensity contrast curves with the FEM-determined strain energy density [Eq. (11)]. Decoupled FEM analysis is used here and the shock pressure is determined from the coupled model. *Figure 18a* shows that they match very well for the single-line shock case, and *Figure 18b* shows they exhibit a similar pattern for the three-line shock case. The agreement is expected, but to further understand the correlation it is important and interesting to explore the strain coupling status at the thin film and substrate interface. *Figure 19* illustrates the variation of individual strain components in (a) the 1 μm thin-film copper and (b) the silicon substrate at their interface determined by the FEM simulation. In copper, the normal strains *E11*, *E22*, and *E33* are dominant as compared with the shear stresses. In-plane strains *E11* and *E22* are both compressive and have a similar magnitude to each other, which indicates an equibiaxial plane-strain distribution. The depth-direction strain, *E33*, is tensile according to the volume conservation through Poisson's ratio and consistent with the maximum principal elastic strain. Across the interface, a corre-

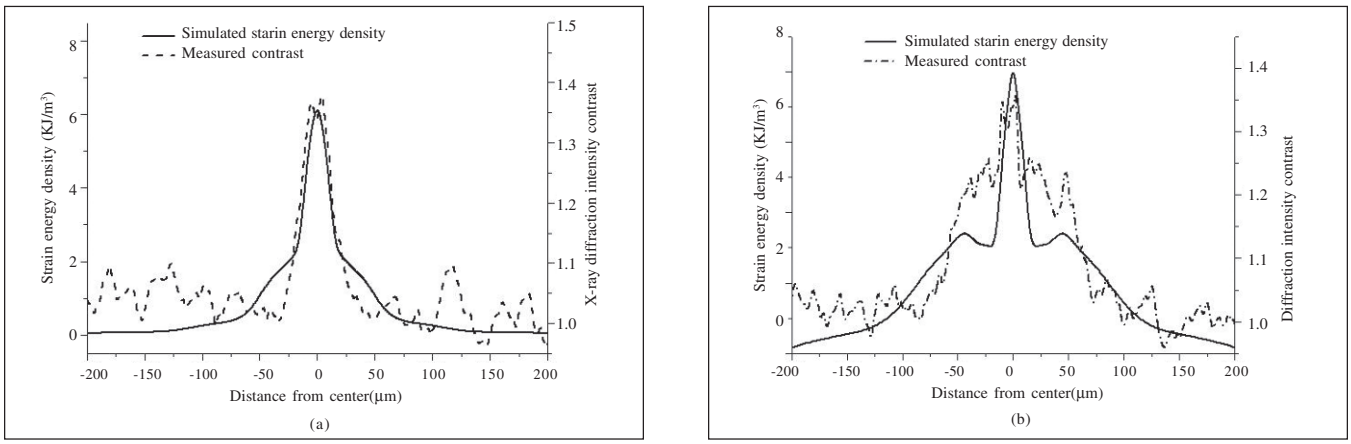

Figure 18
Comparison of Simulated Strain Energy Density and X-Ray Diffraction Intensity Contrast Measurement. (a) Shocked along a single line and (b) shocked along three parallel lines with 50 μm spacing (1 μm thick thin-film sample and 280 μJ laser pulse energy).

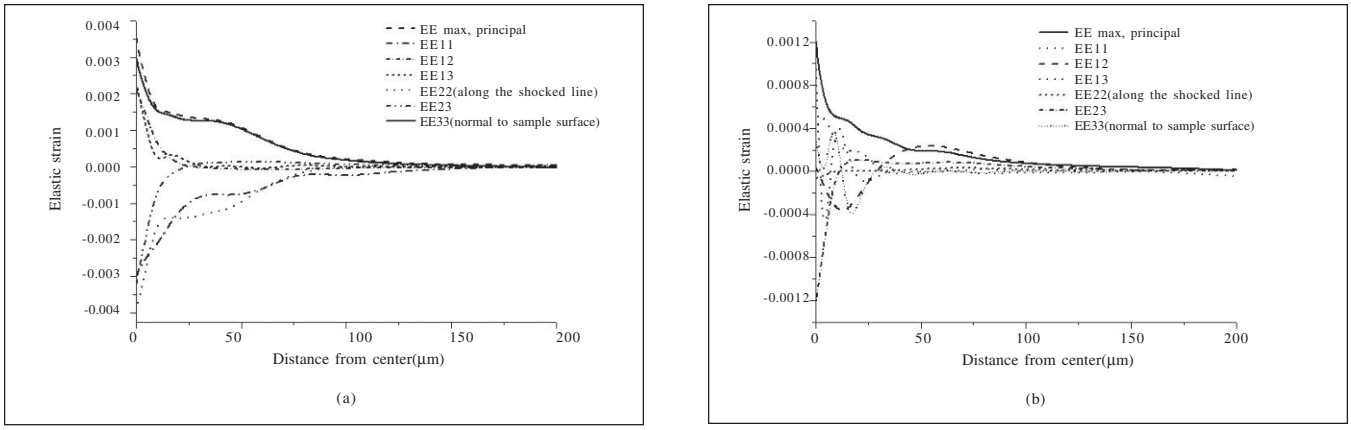

Figure 19
Strain Coupling at Copper-Silicon Interface, 1 μm Thin-Film Sample Shocked at 350 μJ. (a) Variations of elastic strain components in copper across shock region and (b) variations of elastic strain components in silicon across shock region.

sponding strain field balancing the residual stress in the copper layer exists in the silicon layer. From *Figure 19b*, it is clear that in silicon the normal strains are smaller compared with the shear strains. As mentioned before, the shear stress or shear strain in silicon is due to the nonuniformity of stress/strain in the copper layer at the interface. Silicon has a higher Young's modulus than copper so that the strain values in the silicon are smaller than that in the copper under the same level of stress.

From the analysis above, it is clear that elastic strain concentration exists in the silicon substrate through the strain coupling across the interface and it causes the silicon deform in the shock-affected region. This deformation will change the initially perfect single crystal to an imperfect single crystal so that X-ray diffraction intensity increases in this shock-affected region. The width of the maximum principal elastic strain, which is consistent with the distribution of the elastic strain concentration in the silicon, is around ±50 μm, the same as the width from the X-ray diffraction intensity result.

6. Conclusions

Three modeling schemes were considered: (1) coupled analysis based on Model 2, (2) decoupled analysis based on Model 1 and FEM, and (3) decoupled analysis based on Model 2-determined shock pressure as loading in FEM. Due to the limitation of the measurement method and the sample geometry, the plasma temperature and pressure were not measured directly by spectroscopic measurements and a quartz crystal sensor, and the residual strain measurement through X-ray microdiffraction

was used to verify the model. Strain measurements based on the diffraction intensity contrast method agreed with the strain energy density determined by modeling scheme 3, indicating the scheme may represent a good compromise in capturing the physics of microscale LSP. Shock pressure obtained from scheme 1, which considered the dynamic evolution of plasma and the complete physical interaction in laser shock process, has a higher amplitude and lasts longer as compared with that from scheme 2. This is likely to be correct because scheme 2 assumed that part of the laser energy was used to break down water, while this is true only when the laser intensity is very high. An advantage of scheme 1 is that many transient quantities, such as shock and particle velocity, can be directly obtained. Results show the dynamic deformation is much larger if obtained under scheme 1, which assumed that the target deformation under shock is hydrodynamic; under the other two schemes, the FEM simulation considered the target response as a finite-plastic process, and the material strength effect was included. This is likely to be incorrect because the particle and shock velocity of the target material (copper) determined through the FEM in schemes 2 and 3 are consistent with the tabulated Hugoniot data. Shock-pressure attenuation along the target depth direction determined by scheme 1 is smaller than the normal stress (in depth direction) attenuation predicted by the FEM simulation under the other two schemes. As a result, more clear shock fronts were found under scheme 1.

Acknowledgment

This work is partially supported by the National Science Foundation under grant DMI-02-00334. Support by Columbia University is gratefully acknowledged. Valuable discussions with Dr. W. Zhang of GE Global Research Center are also greatly appreciated. HYADES code was made available through Cascade Applied Sciences, Inc. Dr. I. Cev Noyan of IBM Watson Research Center provided guidance and permission to access X-ray microdiffraction apparatus at the National Synchrotron Light Source at Brookhaven National Laboratory.

Appendix

Numerical values of parameters:

h = 6.626×10^{-34} J sec
Planck's constant
k = 1.381×10^{-23} J /° K
Boltzmann's constant
c = 2.998×10^{8} m sec^{-1}
Velocity of light
λ = 355 nm
Laser wavelength
Q_1 = 1×10^{-36} cm^5
Cross section of electron-neutral collision
g_1 = 1
Gaunt factor that corrects the semiclassical expresion for quantum effects
U = 5.989 eV (Al)
Ionization potential of the target material (Al coating)
m_e = 9.110×10^{-31} kg
Mass of the electron
m = 26.981539 amu (Al)
Mass of the target particle
1 amu $\approx 1.6605402 \times 10^{-27}$ kg

References

Asay, J.R. and Shahinpoor, M. (1992). *High-pressure Shock Compression of Solids*. New York: Springer-Verlag, p379.

Berthe, L.; Fabbro, R.; Peyre, P.; and Bartnicki, E. (1998). "Experimental study of the transmission of breakdown plasma generated during laser shock processing." *The European Physical Journal of Applied Physics* (v3), pp215-218.

Berthe, L.; Fabbro, R.; Peyre, P.; and Bartnicki, E. (1999). "Wavelength dependent of laser shock-wave generation in the water-confinement regime." *Journal of Applied Physics* (v85, n11), pp7552-7555.

Boslough, M.B. and Asay, J.R. (1992). "Basic principles of shock compression." *High-pressure Shock Compression of Solids*. New York: Springer-Verlag, pp20-25.

Chou, P.C. (1972). *Dynamic Response of Materials to Intense Impulsive Loading*. published, pp2-5.

Clauer, A.H. and Holbrook, J.H. (1981). "Effects of laser induced shock waves on metals." *Shock Waves and High Strain Phenomena in Metals – Concepts and Applications*. New York: Plenum, pp675-702.

Cullity, B.D. (1978). *Elements of X-ray Diffraction*, 2nd ed. London: Addison-Wesley Publishing Co., pp103, 268-270.

Fabbro, R.; Fournier, J.; Ballard, P.; Devaux, D.; and Virmont, J. (1990). "Physical study of laser-produced plasma in confined geometry." *Journal of Applied Physics* (v68, n2), pp775-784.

Fowles, G.R. (1960). "Attenuation of the shock wave produced in a solid by a flying plate." *Journal of Applied Physics* (v31), pp655-661.

Fox, J.A. (1974). "Effect of water and paint coatings on laser-irradiated targets." *Applied Physics Letters* (v24, n10), pp461-464.

Guy, M.W. (1989). "Physics of laser-induced breakdown: an update." *Laser-induced Plasmas and Applications*. New York: Marcel Dekker, pp48-49.

Hyades (2001). HYADES Professional and HYADES Professional Plus. Cascade Applied Sciences, Inc.

Miller, S.L.; Rodgers, M.S.; LaVigine, G.; Sniegowski, J.J.; Clews, P.; Tanner, D.M.; and Peterson, K.A. (1998). "Failure modes in surface micromachined micro-electro-mechanical actuators." IEEE 98 CH36173. 36th Annual Int'l Reliability Physics Symp., pp17-25.

Mitchner, M. and Kruger, Charles H. (1973). "Collisional and radiative process." *Partially Ionized Gases*. New York: John Wiley & Sons, pp75-79.

Noyan, I.C.; Jordan-sweet, J.L.; Liniger, E.G.; and Kaldor, S.K. (1998). "Characterization of substrate/thin-film interfaces with X-ray microdiffraction." *Applied Physics Letters* (v72, n25), pp3338-3340.

Peyre, P.; Scherpereel, X.; Berthe, L.; and Fabbro, R. (1998). "Current trends in laser shock processing." *Surface Engg.* (v14, n5), pp377-380.

Peyre, P.; Merrien, P.; Lieurade, H.P.; and Fabbro, R. (1995). "Laser induced shock waves as surface treatment for 7075-T7351 aluminum alloy." *Surface Engg.* (v11), pp47-52.

Que, L.; Park, J.S.; Li, M.H.; and Gianchandani (2000). "Reliability studies of bent-beam electrical-thermal actuators." IEEE 00 CH37059. 38th Annual Int'l Reliability Physics Symp., pp118-122.

Robert, G.R. (1989). "Modeling of post-breakdown phenomena." *Laser-induced Plasmas and Applications*. New York: Marcel Dekker, pp72-75.

Tanner, D.M.; Walraven, J.A.; Helgesen, K.S.; Irwin, L.W.; Gregory, D.L.; Stake, J.R.; and Smith, N.F. (2000). "MEMS reliability in a vibration environment." IEEE 00 CH37059. 38th Annual Int'l Reliability Physics Symp., pp139-145.

Ventsel, E. and Krauthammer, T. (2001). *Thin Plates and Shells: Theory, Analysis and Applications*. New York: Marcel Dekker, p37.

Vertes, A.; Juhasz, P.; Dewolf, M.; and Gijbels, R. (1989). "Hydrodynamic modeling of laser plasma ionization processes." *Int'l Journal of Mass Spectrometry and Ion Processes*, pp63-85.

White, R.M. (1963). "Elastic wave generation by electron bombardment or electromagnetic wave absorption." *Journal Applied Physics* (v34), pp2123-2124.

Zhang, W. and Yao, Y.L. (2000a). "Improvement of laser induced residual stress distributions via shock waves." *Proc.* of ICALEO'00, Laser Materials Processing (v89), ppE183-192.

Zhang, W. and Yao, Y.L. (2000b). "Micro scale laser shock processing of metallic components." *ASME Journal of Mfg. Science and Engg.* (v124, n2), pp369-378.

Zhang, W. and Yao, Y.L. (2001a). "Feasibility study of inducing desirable residual stress distribution in laser micromachining." *Trans. of the North American Manufacturing Research Institution of SME* (v29), pp413-420.

Zhang, W. and Yao, Y.L. (2001b). "Modeling and simulation improvement in laser shock processing." *Proc.* of ICALEO'01, Section A.

Zhang, W. and Yao, Y.L. (2002). "Micro scale laser shock penning of metal thin film." *ASME Journal of Mfg. Science and Engg.*, to be summated.

Authors' Biographies

Hongqiang Chen is a PhD candidate in the mechanical engineering department at Columbia University. He received a BS in 1997 and an MS in 2000 in mechanical and electrical engineering from the University of Science and Technology of China (USTC), P.R. China. His research interests are laser materials processing and laser manufacturing. He is a student member of ASME.

Y. Lawrence Yao is a professor in the Dept. of Mechanical Engineering at Columbia University. He received his PhD from the University of Wisconsin-Madison in 1988. He currently serves on the board of directors of the Laser Institute of America and on the board of directors of the North American Manufacturing Research Institute of the Society of Manufacturing Engineers. He and his team in the Manufacturing Research Laboratory (MRL) are interested in multidisciplinary research in manufacturing and design, nontraditional manufacturing processes, laser materials processing, industrial manipulators in manufacturing, and monitoring and fault diagnosis of manufacturing processes and machinery.